About the automatic measurement of the dislocation density obtained by R-ECCI

J. Gallet [a],[*], M. Perez [a], S. Dubail [b], T. Chaise [c], T. Douillard [a], C. Langlois [a], S. Cazottes [a]

[a] Université de Lyon, INSA Lyon, UCBL, MATEIS, UMR CNRS, 5510, France
[b] Axon Square SAS, 4 la Tuilière, 74140 Sciez, France
[c] Univ Lyon, INSA Lyon, CNRS, LaMCoS, UMR5259, 69621 Villeurbanne, France

ARTICLE INFO

ABSTRACT

A proof of concept of a new method for automatic characterization of the dislocation density from scanning electron microscopy images is presented. A series of backscattered electron images are acquired while the sample is rotated. For each pixel of the region of interest, the variation of the grey-level intensity as a function of the rotation angle, called the intensity profile, is calculated. This profile can be used to determine the nature of each pixel (dislocation, matrix or noise), such that an automatic dislocation density can be determined within the region of interest. The method is well adapted for dislocation densities ranging from 10^{12} to 10^{14} m^{-2}. The simulation of a volume containing dislocations enabled the determination of the maximum and minimum densities attainable as well as the theoretical and experimental measurement errors related to the projection of this volume on a two-dimensional image. The theoretical measurement error due to the projection of dislocation on a surface, is 3% for low dislocation densities (10^{12} m^{-2}) and 20% for higher dislocation densities (10^{14} m^{-2}). Experimentally, measurement errors are limited by image analysis conditions, which leads to total measurement errors of 15% for 10^{12} m^{-2} and 34% error for 10^{14} m^{-2}. These uncertainties were obtained considering a given analyzed depth value, that could not be experimentally verified. This uncertainty on the depth value leads to large errors bars in the final measurement, which can reach an order of magnitude.

1. Introduction

Microstructure and dislocations in particular greatly affect the mechanical properties of metallic materials [1]. For example, Blaizot et al. showed the effect of dislocation density on the yield strength of Ni-based superalloys [2,3], and Diano et al. demonstrated that tensile properties are mainly controlled by the grain size and dislocation density [4]. Therefore, it is necessary to accurately characterize these values.

Several methods can be used to determine the dislocation density. One of the most commonly used approaches is to apply the intercept method [5] on transmission electron microscopy (TEM) images. It consists in drawing lines of a known length on an image and counting the number of intersection between those lines and the dislocations present in the image. Another possibility is to get the dislocation density from the crystal distortion using X-ray diffraction (XRD) experiments [6] *via* the broadening of diffraction peaks. Similarly, the crystal deformation can be deduced from Kikuchi pattern distortion calculation (high-resolution electron backscattered diffraction, HR-EBSD), and

disorientation maps can be correlated to local dislocation density estimation [7]. However, there is a lack of information regarding accuracy, and these methods are rarely compared with each other, making it impossible to know which method is to be preferred depending on the subject studied. The ability to image dislocations represents an advantage over other observation techniques because it allows the description of heterogeneous microstructures (multiphase or with different grain sizes for example). However, the main uncertainty of dislocation imaging methods is in the determination of the explored volume. The projection of the explored volume on a two-dimensional image also raises questions about the accuracy of the measurement depending on whether the dislocation is perpendicular or parallel to the surface. When determining the dislocation density, either from TEM or scanning electron microscopy (SEM) images, the visible dislocations present in a given volume are projected onto the image. The dislocation density is defined as $\rho = \frac{L}{V}$, where L is the total length of the dislocation in the volume V. Determination of the analyzed volume for electron channeling contrast imaging (ECCI) in SEM measurements is difficult, and

* Corresponding author.
E-mail address: julien.gallet@insa-lyon.fr (J. Gallet).

the value is often approximated as several times ξ_{hkl} (the extinction distance), which corresponds to approximately a few tenths of a nanometer for steel at 20 kV [8].

Using the SEM, a method currently called electron channeling contrast imaging (ECCI), has been studied by calculation for the first time by Clarke [9]. Almost ten years later, Morin et al. [10], revealed that dislocation contrast in SEM follow similar rules as dislocation imaging in the TEM, especially the fact that the sample must be orientated in a suitable 'Two Beam' condition so that dislocations can be visible. ECCI images were then performed using a high tilt set-up (60–70° tilt) [10], with a dedicated SEM detector positioned aside. Later on, the possibility of performing ECCI with conventional pole-piece mounted detector, and a low sample tilt, was first proposed by Simkin [11], and is nowadays the most popular set-up for ECCI acquisitions. In this mode, dislocations near the surface of a bulk material [12,8] were successfully observed using SEM combined with electron channeling contrast. Its advantage lies in the fact that the observed areas are large and that the sample preparation is much simpler than for TEM. Even if the spatial resolution is lower than that achieved by TEM, it remains sufficient to observe the dislocations [14]. Moreover, it has been shown that *via* the ECCI imaging method, it is possible to obtain dislocation densities [15,16].

In order to reach suitable orientation conditions, ECCI imaging has long been performed using Selected Area Contrast Patterns, often requiring monocrystals or large grains, due to their relatively small spatial resolution. Several improvements of the ECCI method were later proposed. For instance, C-ECCI (for ECCI under controlled diffraction conditions) developed by Zaefferer et al. in 2014 [8], is based on an in-house-developed software called ToCA that calculates the tilt and rotation angles needed to achieve the target two-beam conditions using input data from the electron backscattered patterns. Mansour et al. developed another variant called A-ECCI (Accurate-ECCI) in 2014 [17]. However, this method requires a special installation in the scanning electron microscope to perform portions of the electron channeling patterns (ECP) acquisition in "rocking beam" mode. Finally, there is also the R-ECCI method (Rotation-ECCI) developed by L'hôte et al. in 2017 [18]. This method is based on the recording of a series of images during the rotation of the sample. For each pixel of the region of interest (ROI), the variation of intensity as a function of the rotation angle is obtained and called an intensity profile. This intensity profile contains information on the pixel orientation[19] but also on the nature of the considered pixel (noise, or grain boundary, matrix or dislocation) [20]. Therefore, by applying a dedicated algorithm, it is possible to automatically determine the dislocation density using these intensity profiles. This methodology was successfully applied to a non-deformed steel, and a density of 3×10^{13} m^{-2} was obtained. However, the uncertainty of the measurement and limitations of the methodology were not clearly defined. Moreover, the clustering algorithm used for this proof of concept was not adapted for deformed grains, which would exhibit internal disorientation, as often the case after deformation.

In the current work, a new dislocation detection algorithm was developed, with the aim of better characterizing grains that would exhibit internal disorientation caused by the presence of dislocations. This new method has been applied for a duplex stainless steel for different deformation levels. Then, the reliability and possibilities, such as the maximum and minimum achievable densities, were characterized. First, a theoretical review of the uncertainty factors is presented, and then, some parameters are studied theoretically in detail, such as the effect of the analyzed volume projection and the effect of dislocation overlap. Then, the effect of the clustering algorithm is presented. The general conclusions are finally verified on the experimental data. In this study, the expected dislocation densities on undeformed and deformed steels are between 10^{13} and 10^{14} m^{-2}, as in the study by Ruggles et al. [14].

2. Materials and methods

The SEM observations were performed on a Zeiss Supra 55VP SEM with an accelerating voltage of 20 keV using a 120-μm diaphragm and a working distance of ~7 mm. The SEM images were recorded with a pixel size of 4.5–6 nm and a size of 1024 × 768 pixels.

2.1. Materials

Observations were made on a commercial Outokumpo 2101 lean duplex stainless steel that was mechanically ground, with final polishing was performed using a 1-μm diamond solution. To avoid any strain hardening of the surface, a final electropolishing step was performed using an A2 electrolyte (from Struers APS, Denmark) at 20 V for 60 s with the Lectropol 5 device (Struers APS, Denmark).

The evolution of the dislocation density was characterized in both ferritic and austenitic phases. Micro tensile samples (total length 112.5 mm, width 12.5 mm, and thickness of 1.5 mm) were deformed using a MTS tensile machine. Standard digital image correlation (DIC) was used to follow and precisely measure the deformation of each point of the sample surface. One sample was deformed up to 3% and the other one up to 10%. Then, R-ECCI was applied to several grains for each deformation state. Fig. 1 presents isolated images of the rotation image series that reveal the dislocation structure for undeformed and 10% deformed ferrite, Fig. 1 (a) and (c), respectively, and for undeformed and 3% deformed austenite, Fig. 1 (b) and (d), respectively.

In the undeformed state, dislocations in ferrite appear as dots or lines on the image, indicating that their orientation relative to the surface is quite random. The matrix is not completely dark and appears quite noisy. The contrast of vertical dislocations (appearing as dots) is greater than that of the horizontal dislocations. A large white zone is observed that could originate from the presence of a large defect or a polishing artifact that was not considered in the data treatment. After deformation, more tortuous dislocations appeared in the ferrite grains as well as more dot dislocations. In the grain presented in Fig. 1c, the bottom part of the grain is in good condition of dislocation imaging (dislocations appear white on a dark matrix), while the top part of the grain appears bright and dislocations are not visible. This is due to the local disorientation that appeared during deformation, the orientation of the grain is not similar on its top and bottom part. Therefore, the orientation of the sample required to image dislocation is not the same for the bottom and top part. This reveals one of the major advantages of using intensity profiles instead of single images for the determination of dislocation densities, as already presented in [18]. In the rotation image series, all part of the grains will become suitably oriented but not for the same rotation angle. Therefore, using an adapted clustering algorithm, it is possible to detect dislocations in all part of the grains, even if a slight disorientation is present within the grain.

For austenite grains in the as received condition, Fig. 1(b), few dislocations are present, the matrix is homogeneously dark, and dislocations present a very high contrast. However, after only 3% of deformation, the amount of dislocations in the austenite phase is very high, dislocations are very long and linear, and appear aligned along {111} type planes. This high dislocation density is expected as austenite deforms before ferrite in duplex stainless steels. In this case a distortion of the grain in also present, which explains the fact that the top right and left part of the grain are very bright, while the bottom remains in diffraction condition. The apparent density is so high that dislocation might overlap within the analyzed volume, which would lead to uncertainties in the density measurement.

2.2. Acquisition method

When the grain is in appropriate diffraction condition for dislocation imaging (called two-beam (TB) condition), dislocations appear white on a dark background. To do this, the sample must first be tilted by few
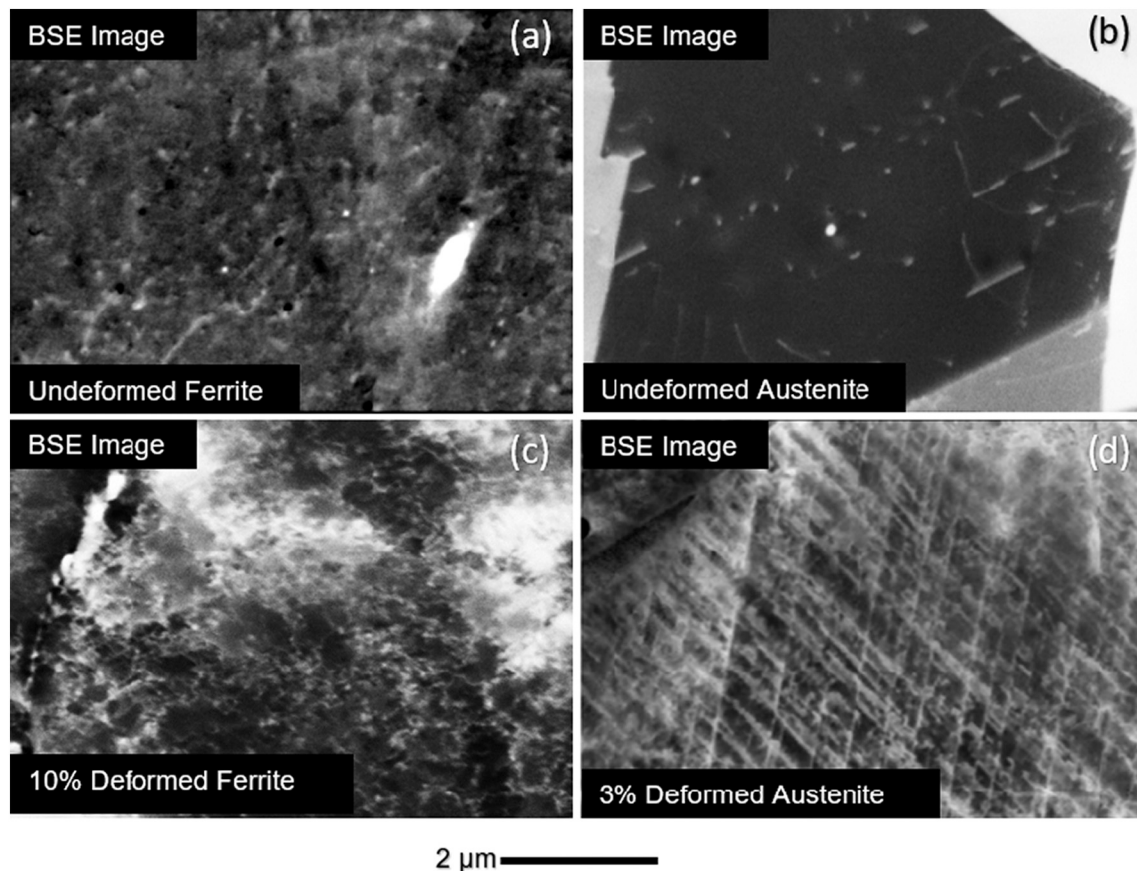
Fig. 1. BSE image extracted from the series acquired on different grains. For each image, the dislocation lines are visible in white on a black background. Each image was acquired with an acceleration voltage of 20 keV with a pixel size of 4.5 nm and an aperture of 120 μm. (a) Undeformed ferrite grain. (b) Undeformed austenite grain. (c) 10% deformed ferrite grain. (d) Austenite grain deformed at 3%, where dislocations are visible.

degrees and rotated by 360°. A backscattered electron (BSE) image is acquired at each rotation step, such that 180 or 360 images are recorded, for 1° or 2° rotation steps, respectively. During the rotation, the orientation of a given pixel describes a circle on the selected grain's electron channeling pattern (ECP). The radius of this circle corresponds to the selected tilt angle. It was shown that, regardless of the grain orientation, this circular crystallographic path crosses several Kikuchi bands; therefore, several rotation angles will correspond to adequate diffraction condition for dislocation imaging, *i.e.*, at the Kikuchi band edges [20]. For a large tilt angle, the circle diameter will be larger and more diffraction bands will be crossed. However, that can lead to some geometrical difficulties within the chamber during the sample rotation; the sample might be touching one of the present detectors. A tilt angle of 5°–10° appears to be the best compromise to cross a sufficient number of bands without any danger for the detectors.

This procedure is automated using a rotation sub-stage, together with the use of a program that acquires an image after each rotation step, developed in the framework of the e-CHORD project [19]. For dislocation imaging, the magnification required is high (minimum 5 nm/pixel), and the image quality is sensitive to a perfect astigmatism or focus setting. However, each image acquisition takes approximately 1 min 30 s, and a drift in the focus/astigmatism together with a mechanical drift of the sample occur along the rotation and time. It is thus necessary to refocus and recenter the ROI by hand every 5–10 images.

To avoid this issue, it is possible to limit the observations to angular ranges that correspond to the diffraction conditions for dislocation imaging. It is then possible to switch from a series of images over 360° to several "mini-series" of 20° to 30° each, located near local minima. A preliminary complete series at very low magnification is first acquired

over 360°. For each pixel of the ROI, the grey-level intensity is plotted as a function of the rotation angle to obtain a so-called "intensity profile". This complete series is used to identify the angular ranges for each grain where dislocations can be observed. The angular ranges corresponding to dislocation contrast conditions are the minimum of this intensity profile (see Cazottes et al. [20]).

A pixel clustering method based on the analysis of the contrast variation between the dislocations and the grain-matrix profiles allows an automatic determination of the dislocation density [20].

2.3. Adaptation of the clustering algorithm for distorted grains

The clustering is divided into two steps. The first step consists of partitioning [21–23] the elements to be classified, *i.e.*, grouping all the elements contained in the same grain. The second step is the classification [24,25], which consists of identifying each of the elements constituting these partitions (grains), *i.e.*, identifying dislocation pixels, matrix pixels, and noise pixels. Indeed, the pixels located on a dislocation present an identical profile as one of the pixels located on the grain, except for the diffraction condition, for which the dislocation appears bright and the matrix dark [8,20].

The partitioning step presented in Cazottes et al. [20] was based on the calculation of the difference between a considered pixel profile and the average profile of the grain. If the difference between the two profiles is too high, the pixel is not considered to be part of the grain. However, for a deformed grain, an internal disorientation can appear. In that case, profiles from adjacent pixels will still be close; however, profiles from further pixels might differ, although they are part of the same grain.

Fig. 2 presents an austenitic grain deformed grain at 35%. It is possible to observe several areas with different observation conditions. Zone A is under suitable observation conditions for the dislocations; therefore, the dislocations are visible in white on a black background. However, a few hundred nanometers around, it is no longer the case: zone B is outside of these observation conditions. It is not very far from its observation condition as the dislocations are still barely visible. Finally, zone C, located further away, is completely out of the observation conditions. In this area, the grain is completely white and the dislocations are not visible. These findings are similar to the results presented in Fig. 1, where for higher deformation levels, the distortion leads to different diffraction conditions throughout the grain. Therefore, a comparison with the average profile of the grain is no longer relevant on deformed materials. It is then necessary to modify the profile comparison strategy using a more local average profile around the analyzed pixels.

The algorithm was changed such that the analyzed pixel intensity profile is compared with a local average of intensity profiles around it. The number of neighbors selected for the average is selected, with the variable b called the "bin size" (see Fig. 3). If the analyzed pixels are located at the edges of the image, the area is cropped, and the average is obtained on a reduced number of pixels.

For profile comparison, the intensity profiles were then transformed into vectors. The intensity profile of a pixel located at (i,j) will be transformed to the vector $\overrightarrow{P_{(i,j)}} = (x_1, x_2, \ldots x_N)$ of dimension N, N being the number of images contained in the stack and the x_i values being the intensity in grey level of the pixel (i,j) for the image N.

If mini-series are used, then the vector $\overrightarrow{P_{(i,j)}}$ used for comparison of the intensity profiles will have a dimension N' smaller than that of a complete series, thus decreasing the necessary calculation time previously presented in [20]. The distance $D\left(\overrightarrow{P_{i,j}}, \overrightarrow{P_{k,l}}\right)$ between the vectors contained in b and the central point of the bin size (Fig. 3) is calculated using an Euclidean difference:

$$D\left(\overrightarrow{P_{i,j}}, \overrightarrow{P_{k,l}}\right) = \left\| \overrightarrow{P_{i,j}} - \overrightarrow{P_{k,l}} \right\|. \tag{1.1}$$

For very diffuse dislocations or for noisy images, normalizing the $P_{i,j}$ vectors can improve the results. In the studied case, the Euclidean
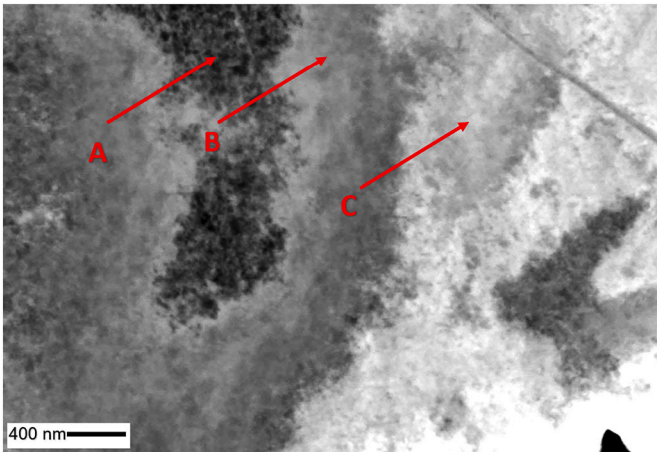

Fig. 2. Example of a BSE image acquired with an acceleration voltage of 20 keV, an aperture of 120 μm, and a pixel size of 4.5 nm and obtained on a 35% deformed austenite grain. The important disorientation in the grain generates three different zones: (a) a zone where the dislocations are in observation conditions; (b) the disorientation of the grain moves away from the observation conditions, which reduces the contrast between the dislocations and the grain; and (c) the observation conditions of the dislocations are lost, and the dislocations are no longer visible.

normalization was used: $\overrightarrow{P}' = \dfrac{\overrightarrow{P}}{\sqrt{\sum P_i^2}}$.

Then, to enable the detection of pixels that have sufficient profile variations to be potential defects, a value d_b, representative of the mean distance between this pixel and its environment, is calculated. For each pixel (i,j), surrounded by $b^2 - 1$ neighbors (see Fig. 3):

$$d_b(i,j) = \frac{1}{b^2} \sum_{(i',j') \ neighbor \ of \ (i,j)} D\left(\overrightarrow{P_{i,j}}, \overrightarrow{P_{i',j'}}\right) \tag{1.2}$$

A map, called "Features", represents the areas for which d_b exceeds a certain threshold d_t and highlights the defects in green (Fig. 4(b)).

This "Features" map (Fig. 4(b)) shows areas containing local "anomalies" with respect to the profiles contained in the stack. These anomalies may be dislocations but also dust, grain boundaries, or other defects that locally affect the contrast. All anomalies (dislocation and noise pixels) are placed in a set named K_{roi} (roi stands for region of interest). All the other pixels are considered matrix pixels.

2.4. Noise detection

This step aims to distinguish dislocations from other defects within K_{roi}. Defect pixels are stored in a cluster called K_{dp} (dp stands for "discarded pixels"). The assumption here is that the difference in the intensity profile of a discarded pixel and the local matrix or dislocation profiles will be large regardless of the angle and orientation condition. It represents the fact that a defect (dislocations excluded) is always visible on all images of the series. In contrast, dislocations become visible only for particular angles, which correspond to the visibility conditions.

For this purpose, it is first necessary to group the different pixels contained in K_{roi} into different "objects", formed by percolating pixels of K_{roi}. Let K_{ol} be the ensemble of pixels of an object of index l. Small objects containing less that n_p pixels, which cannot be dislocations, are automatically discarded and their pixels are put in the "discarded pixel" cluster.

Around each object, we define a local area of the matrix, called the matrix margin (mm), that will be used to calculate the average local profile of the matrix $\overrightarrow{P_{mean}^l}$. The matrix margin area around each object is defined by the sum of matrix pixels contained within a circle of radius b_m centered on all pixels of the object. All pixels lying in the Matrix Margin of object l are included in a region named K_{mm}^l:

$$\forall (i,j) \in K_{o_l}, \text{for all pixels } (i',j') \notin K_{roi} \text{ such that } (i-i')^2 + (j-j')^2 < b_m^2 \tag{1.3}$$

$$(i',j') \in K_{mm}^l \tag{1.4}$$

The average local profile of the matrix $\overrightarrow{P_{mean}^l}$ around object l is defined as

$$\text{For all } (i,j) \in K_{mm}^l, \overrightarrow{P_{mean}^l} = \left(\bar{x}_{ij1}, \bar{x}_{ij2}, \ldots, \bar{x}_{ijN}\right). \tag{1.5}$$

For the sake of illustration, Fig. 6(b) shows the matrix margin region (white pixels) around the object indicated by the red arrow.

All profiles of all pixels of the image are then normalized (profiles with a prime (') represent normalized profiles):

$$\overrightarrow{P'_{(i,j)}} = (x'_1, x'_2, \ldots x'_N) \text{ with } x'_n = \frac{x_n - MIN(x_n)}{MAX(x_n) - MIN(x_n)}. \tag{1.6}$$

This normalization decreases the distance between the matrix and dislocation profiles, as illustrated in Fig. 5b. However, the intensity profiles corresponding to noise or artifacts will still have differences over the entire profile that do not change much with normalization. This step allows dislocation pixels to be distinguished from noise pixels contained in the image. For this, the Euclidean distance D of the normalized profile is compared with a value H. The distance D between

Fig. 3. Illustration of the analysis parameter "bin size" with a value of 2, 3, 4, and 5, respectively. The analyzed pixel is shown in light blue, and its neighbors are shown in deep blue. (For interpretation of the references to colour in this figure legend, the reader is referred to the web version of this article.)
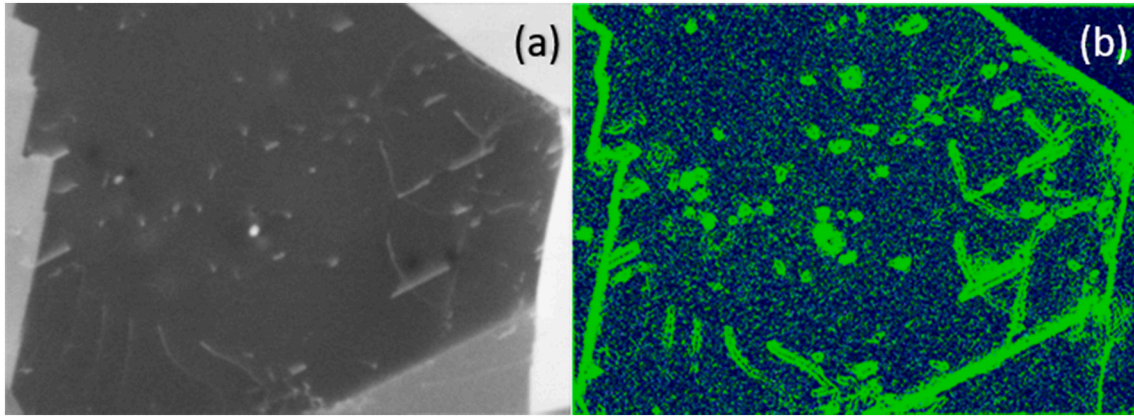

Fig. 4. Example of "Features" map obtained from a series of BSE images of an undeformed austenite grain. (a) BSE image where dislocations appear in white on a black background. (b) Corresponding "Features" map obtained with the profile analysis, which shows in green all the intensity profiles that differ from those of their neighbors. This map was obtained with a bin size of 5 and a threshold d_t equal to the 77th percentile of $d_b(i,j)$.

the normalized profiles of the matrix dislocations will be very small while the distance D between the normalized profiles of the matrix and the other defects will remain large. For each object l,

$$\forall (i,j) \in K_{o_l}, \text{ if } D\left(\overrightarrow{P'^l_{i,j}}, \overrightarrow{P'^l_{mean}}\right) > H \text{ then } (i,j) \in K_{dp}. \quad (1.7)$$

Finally, some other black spots usually appear in the images (see Fig. 5), which correspond to intensity profiles that follow the same trends as the average grain profile and an intensity difference with the local matrix that is too low to be discarded in the previous step. These pixels will be removed under the assumption that the local difference between the matrix and dislocation is necessarily positive (*i.e.,* the dislocations appear white on a black matrix).

$$\forall (i,j) \in K_{O_l} \text{ and} \forall (i',j') \in K^l_{mm}, \text{ if } \left(\text{for all series } n, x_{ijn} < x_{i'j'n}\right) \text{ then } (i',j')$$
$$\in K_{dp} \quad (1.8)$$

2.5. Detection of dislocations

After having discarded noise pixels (see previous section), dislocation pixels are detected by analyzing *separately* the intensity differences near local minima (diffraction condition). Mini-series are extracted from the complete series of image profiles. Each mini-series describes the intensity profile near a local minimum:

$$\overrightarrow{P_{(i,j)}} = (x_1, x_2, \ldots x_N) \rightarrow \overrightarrow{P^1_{(i,j)}}, \overrightarrow{P^2_{(i,j)}}, \ldots, \overrightarrow{P^{N_s}_{(i,j)}}, \quad (1.9)$$

where N_s is the number of observation mini-series.

For each object of index l and each mini-series of index n_s containing N_{n_s} images, we calculate the mean local matrix profile:

$$\text{For all } (i,j) \in K^l_{mm}, \overrightarrow{P^{l,n_s}_{mean}} = \left(\bar{x}^{n_s}_{i'j'1}, \bar{x}^{n_s}_{i'j'2}, \ldots, \bar{x}^{n_s}_{i'j'N_{n_s}}\right). \quad (1.10)$$

For each mini-series of each object l, the difference of the integrals between each pixel of K_{o_l} and K^l_{mm} is calculated. If one or more mini-series exhibits a distance larger than a threshold ε_d, the pixel is considered a dislocation pixel.

$$\forall (i,j) \in K_{o_l} \text{ if one or more mini-series satisfies } \int \overrightarrow{P^{l,n_s}_{i,j}} - \int \overrightarrow{P^{l,n_s}_{mean}} > \varepsilon_D,$$
then $(i,j) \in K_{dislocation}.$

$K_{dislocation}$ is the set of pixels considered as dislocations.

The ε_D value represents the difference necessary for the pixel (i,j) to be considered a dislocation. It is therefore necessary to proceed by iteration from the ECCI images to determine and refine its value.

2.6. Results of the clustering

A so-called « Cluster Map » (Fig. 6) is used to verify the parameters used in the previous analyses.

The excluded profiles (too different from the rest of the grain, grain boundaries, *etc.*) are plotted in black, and the different grains appear with different colors. Moreover, the defects detected *via* the "features" (Fig. 4) appear in the same colour as their corresponding grain but lighter (yellow arrows). In the example in Fig. 6, the pixels located in the lighter zone (yellow arrow) can be compared with the local average of the grain profiles, calculated in a zone around it, whose thickness is equal at B_m, as indicated in white (red arrow).

In the BSE images presented in Fig. 1, dislocations appear with a width of several pixels (30-nm width for the steel at this accelerating voltage, *i.e.,* 4–5 pixels wide). However, in Fig. 6, some isolated pixels are detected as potential dislocation pixels. An additional user-defined parameter is used to fix the minimum size of dislocations present in the images to remove the isolated pixels from the dislocation clusters.

Finally, for each mini-series, *i.e.,* each set of orientation conditions, clustered maps are calculated, where the matrix is plotted in dark and the dislocations pixels are shown in green, as shown in Fig. 7.
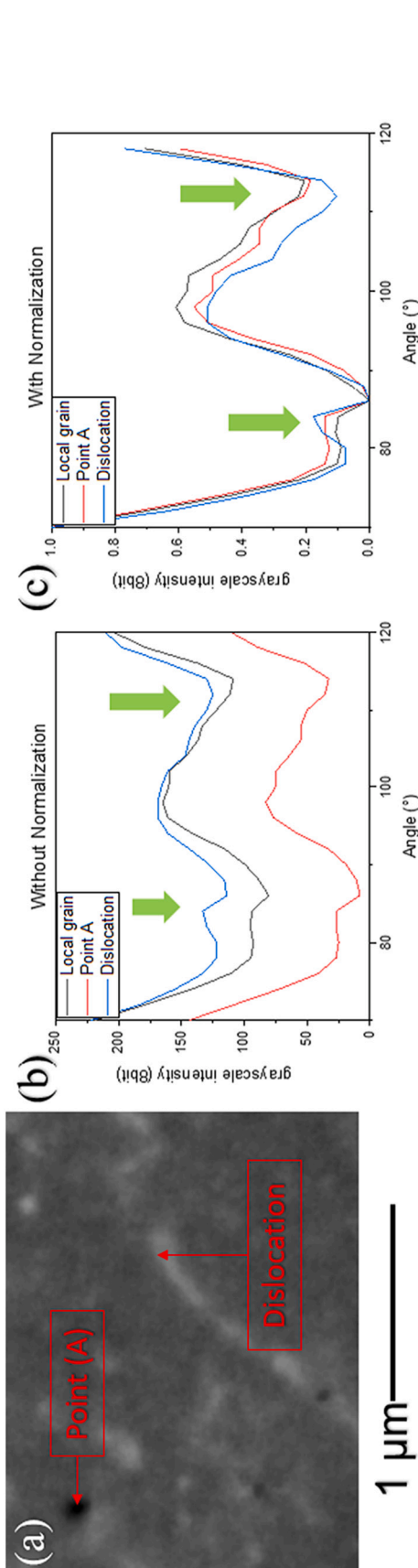
Fig. 5. (a) BSE image of dislocation contained in an undeformed ferrite grain obtained at an accelerating voltage of 20 keV. (b) Intensity profile of the matrix (in black) of a dislocation pixel (in blue) and of a black point (in red) without normalization. The green arrows represent conditions where dislocations are visible in white on a black background. (c) The same intensity profile as (b) with normalization. (For interpretation of the references to colour in this figure legend, the reader is referred to the web version of this article.)

Fig. 7 shows dislocation clusters with thicknesses greater than those in the original BSE image (red arrows, Fig. 7). It is possible to refine the detection parameters to obtain a thinner thickness; however, a loss of information can occur for dislocations that appear with lower contrasts (yellow arrow, Fig. 7). The average thickness of the dislocation must be considered in the calculation of the dislocation density. Indeed, because the dislocations are not thicker than one pixel, counting the total number of green pixels in Fig. 7(b) means counting the same dislocation several times in the measurement of the total length of dislocation lines used in the density calculation. To avoid this, the total number of pixels detected as dislocations is divided by the average thickness of each dislocation, and the pixels contained in the other grains are removed manually before the calculation of the dislocation density. It is possible to remove the number N of dislocations appearing in green in Fig. 7(b) to determine the dislocation density in the image series.

3. Results

Theoretical maximum and minimum measurable dislocation density
Preliminary calculation of the measurable dislocation density
The dislocation density is calculated using the following formula:

$$\rho_{clus} = \frac{L}{V}$$

After data treatment, the total number of dislocation pixels N^{dislo} is determined. The total length of the dislocations is then calculated using

$$L^{dislo} = \frac{N^{dislo} \times P_S}{E} \tag{1.11}$$

With E the mean thickness of dislocations (in pixels), and P_S the pixel size in nm.

$$E = E^{app}/P_S \tag{1.12}$$

With E^{app} the apparent dislocation width in nm.

$$\rho = \frac{N^{dislo} \times P_S}{S \times t \times E} = \frac{N^{dislo} \times P_S 2}{N^{tot} \times P_S 2 \times t \times E^{app}} = \frac{N^{dislo}}{N^{tot} \times t \times E^{app}} \tag{1.13}$$

With t the analyzed sample thickness (in nm), and S the analyzed surface in nm^2. N^{tot} is the total number of pixels on the image. Therefore, the dislocation density ρ only depends on E^{app} measured manually on the image.

The determination of the analyzed thickness is difficult to achieve experimentally. Previous studies [8,25,14] considered that the analyzed thickness depends on the orientation conditions of the sample, and can be approximated as $t = 3. \xi_g$ with ξ_g the extinction distance corresponding to the diffracting vector $\overrightarrow{g}$. This value thus depends on the orientation condition of the sample, and will not be the same for all images of a given series. It will range from 70 nm for austenite in $\overrightarrow{g_{111}}$ orientation, to 115 nm for ferrite $\overrightarrow{g_{220}}$ orientation. For sake of simplification, and for both phases, the analyzed thickness was set to 100 nm for all conditions. The impact of this approximation on the measurement will be discussed later in the text.

However, the observations show that the width of dislocations E^{app} no longer evolves beyond a given magnification. Two images of the same area were acquired on a ferrite grain under the same experimental conditions, one with a pixel size of 4.5 nm (1024 × 768 pixels) Fig. 8 (a) and the other with a pixel size of 2.25 nm (2048 × 1536 pixels) Fig. 8 (b). One can see that there is no difference in the apparent width of the dislocations (27 nm in that case). Therefore, in order to limit acquisition time, all acquisitions performed on this material were made with a pixel size of 4.5 nm.

Considering a pixel size of 4.5 nm and an image size of 1024 pixels × 768 pixels, a theoretical dislocation density was calculated. Arbitrarily, the minimum density was chosen to corresponds to an image where 1% of the pixels are dislocation pixels. Applying Eq. (1.13) leads to a theoretical minimum value of 3.45×10^{12} m^{-2}.

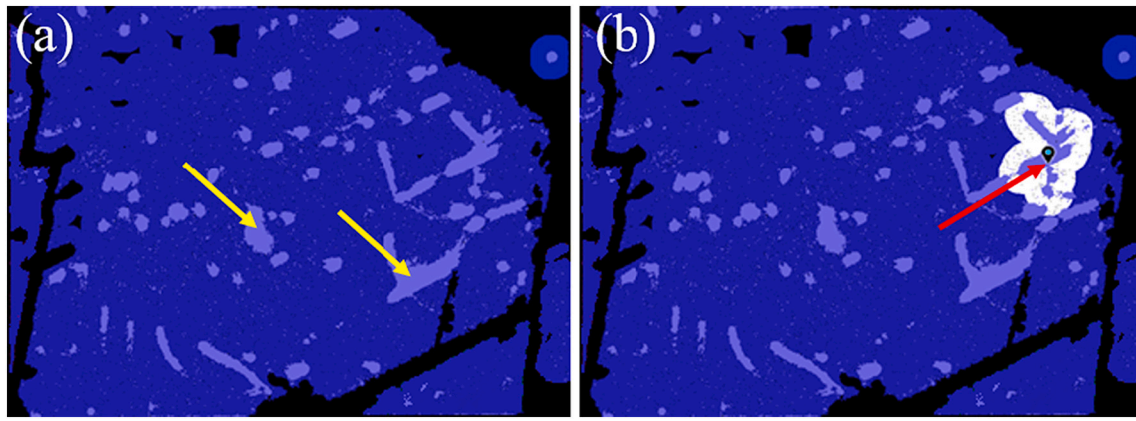On the other end, the maximum density measurable cannot exceed

Fig. 6. Example of Cluster Map obtained on an undeformed austenite grain. (a) The grain appears in dark blue while the areas of interest or potential defects appear lighter in this area (yellow arrows). (b) Illustration of the "Matrix Margin" (Bm neighbors) zone that appears in white and that is used to calculate the local average value of the grain for comparison with the different pixels contained in the zone of interest (red arrow). Cluster map obtained with $b_m = 30 \ pixels$, $\varepsilon_D = 40th \ percentile$. The objects composed of less than 5 pixels were excluded. (For interpretation of the references to colour in this figure legend, the reader is referred to the web version of this article.)
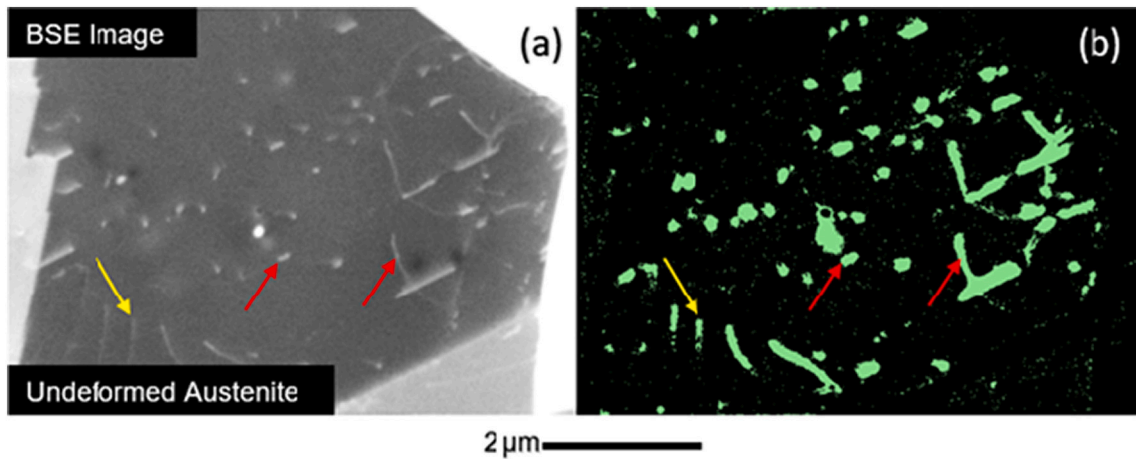

Fig. 7. Example of clustering result (b) with the corresponding BSE image (a), where dislocations are shown in white on a black background. The clustering result shows the pixels detected as dislocations in green on a black background. Some well-defined dislocations on the BSE image (red arrows) appear with large thicknesses in (b) while more diffuse dislocations have comparable thicknesses (yellow arrow). (For interpretation of the references to colour in this figure legend, the reader is referred to the web version of this article.)

the total number of pixels. Arbitrarily, the maximum dislocation density is chosen to corresponds to an image where 50% of the pixels are dislocations pixels. It leads to a maximum theoretical dislocation density of $1.73 \times 10^{14} \ m^{-2}$.

These limits are indicative and should be reconsidered in the light of experimental results and associated measurement bias.

3.1. Experimental measurement of high and low dislocation densities

Two sets of BSE images were acquired for the experimental tests: the first one on an undeformed ferritic grain and the second one on a 3% deformed austenitic grain (Fig. 1 (a) and (d)). The clustering method applied on these two sets of images is presented in Fig. 9, with the dislocation pixels detected in green on a black background. The measured densities are $\rho_{clus} = 5.8 \times 10^{12} \ m^{-2}$ for the undeformed ferritic grain and $\rho_{clus} = 5.7 \times 10^{13} \ m^{-2}$ for the 3% deformed austenitic grain. ρ_{clus} was calculated using the following formula:

$\rho_{clus} = \frac{L}{V}$ with $L = \frac{N_{dislocation}}{E} \times P_s$, where $N_{dislocation}$ is the number of pixels detected as dislocations, E is the average dislocation thickness, and P_s is the pixel size.

In the images, the dislocations have an apparent width of several

pixels, which depends on the observation conditions and the observed material. Using the total number of dislocation pixels in the image, the length of one dislocation is counted several times because of the thickness of several pixels. Therefore, to determine the appropriate length of the dislocation, its apparent length should be divided by its apparent thickness.

Additionally, for validation purposes, the dislocation density was measured on the clustered image presented in Fig. 9 using the $\rho = N/S$ method, which consists of counting the number of dislocations N visible on the image and dividing it by the surface of the image. The density measurements obtained are $\rho_{N/S} = 5 \times 10^{12} \ m^{-2}$ on the undeformed ferritic grains and $\rho_{N/S} = 4 \times 10^{13} \ m^{-2}$ for the austenitic grains deformed at 3%. The difference between these values originates from the different uncertainties of measurement, in particular, the one on the volume which is not considered with the N/S method but also from the overlapping of the dislocations and the fact that it is difficult to really detect everything with the clustering algorithm. However, the measurements are of the same order as those obtained by the clustering method, which validates the last step of the clustering method.
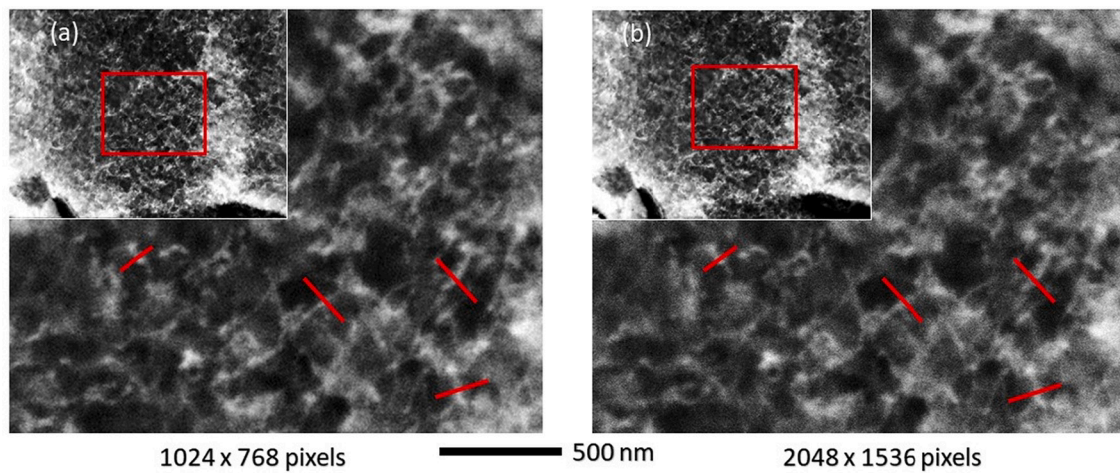
Fig. 8. BSE image acquired on a ferrite grain deformed at about 3%. For each image, the dislocation lines are visible in white on a black background. Each image was acquired with an acceleration voltage of 20 keV, an aperture of 120 μm and an acquisition time of 3.7 min. (a) Ferrite grain observed with a pixel size of 4.5 nm. (b) Same area as image (a) but with a pixel size of 2.25 nm. Dislocation widths were measured perpendicular to the dislocation line. The red lines represent examples where identical widths were measured. (For interpretation of the references to colour in this figure legend, the reader is referred to the web version of this article.)
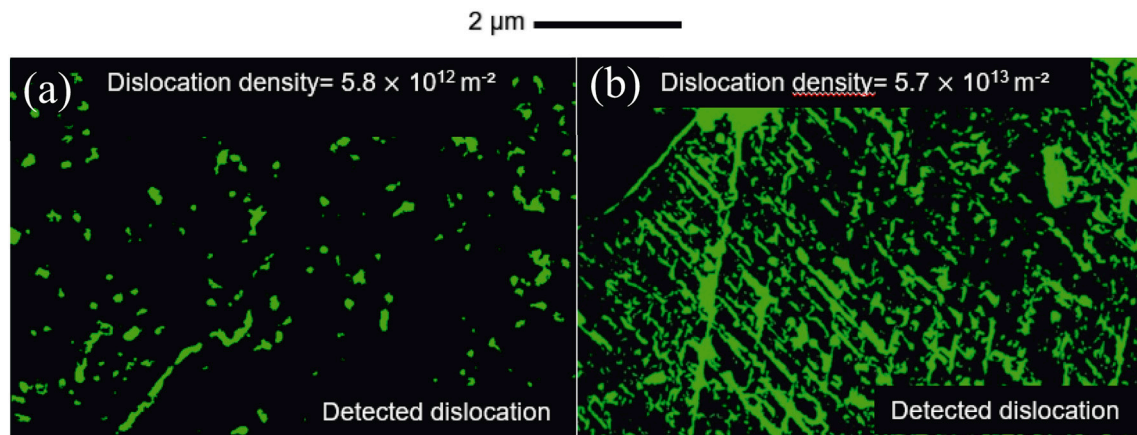

Fig. 9. (a) Clustering image of an undeformed ferrite grain, where dislocations appear in green on a black background. The dislocation density measured on this grain is equal to 5.8×10^{12} m^{-2}. (b) Clustering image of a 3% deformed austenite grain, where dislocations appear in green on a black background. The dislocation density measured on this grain is 5.7×10^{14} m^{-2}. (For interpretation of the references to colour in this figure legend, the reader is referred to the web version of this article.)
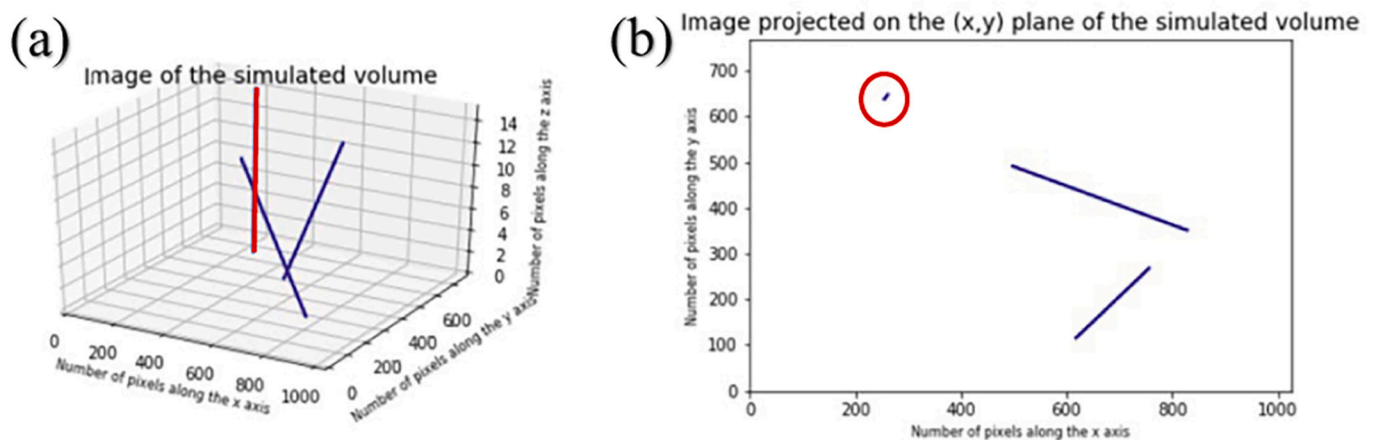

Fig. 10. (a) Example of dislocation (in blue) obtained with a random direction in a three-dimensional volume and a red dislocation that is almost perpendicular to the (X,Y) plane. The simulated volume is comparable to the experimentally explored volume. (b) Projected image of the volume on the (X,Y) plane with the dislocation almost perpendicular to the surface, which appears as a point (red circle). (For interpretation of the references to colour in this figure legend, the reader is referred to the web version of this article.)

3.2. Estimation of the dislocation density measurement error

The dislocation density measurement uncertainty arises from three main factors: the first one is related to the apparent thickness of the dislocation and the selection of the pixel size and magnification, the second one is related to the projection of the 3D analyzed volume onto a 2D image, and the third one is related to the dislocation overlapping.

It is possible to quantify the measurement error from the apparent thickness of the dislocations E. As this value is obtained with a precision of one pixel it is possible to repeat the previous calculations with $E' = E \pm 1$ pixel. These calculations show that this measurement of the average thickness E of the dislocations causes an error of 6%–7% in the measurements.

The second effect that leads to uncertainty in the dislocation density measurement is linked to the projection of the analyzed volume. The apparent length of a given dislocation on the 2D projected surface is highly dependent on its orientation in the analyzed volume. For instance, a dislocation that is strictly parallel to the surface will be counted with its real length, whereas a dislocation perpendicular to the surface (red dislocation, Fig. 10(a)) will appear as a point on the projected image (red circle Fig. 10(b)), and its length will be underestimated.

Volumes containing a given number of dislocations (plotted as straight blue lines, Fig. 10(a) were simulated, and the projections of those dislocations on a 2D image were calculated (Fig. 10 (b)). In the case presented in Fig. 10, the volume and surface sizes were close to those typically required for dislocation images in ECCI (1024 × 768 pixels, a pixel size of 4.5 nm, and a depth of approximately 100 nm). The orientation of the dislocations was randomly selected by taking randomly generated points in the considered volume. A direction was then randomly selected in a sphere around this point to draw a line that entirely crosses the volume.

The real dislocation density was calculated from the 3D volume: $\rho_{real} = \frac{\sum \|d_{3D}\|}{V}$ $\left[\text{m}^{-2}\right]$, where d_{3D} is the total length of each dislocation. To estimate the uncertainty resulting from the projection of these 3D objects on a 2D surface, the projected density was estimated: $\rho_{projected} = \frac{\sum \|d_{2D}\|}{V}$, where d_{2D} is the total projected length of each dislocation. The measurement error M was calculated using the densities obtained with the linear coordinates in 3D and 2D using the relation $M = \frac{\rho_{real} - \rho_{projected}}{\rho_{real}}$, as

plotted in Fig. 11. M increased up to 6% for densities of 2×10^{12} m^{-2} and then fluctuated between 5% and 7% for higher densities values. For the maximum density achievable using the present method, $M = 7\%$. Oscillations in the error measurement are attributed to the random orientation of the generated dislocations. When a dislocation is generated parallel to the projection surface, its contribution to this source of error is zero. In contrast, if it is generated perpendicular to the projection surface, its contribution will be maximum. The rapid increase and fluctuation of the error source for low dislocation densities is attributed to so few dislocations being present in the volume. Thus, each dislocation will have a significant impact of the difference between the real and projected density. However, by increasing the number of dislocations, the proportion of dislocations that are perfectly straight compared with all others is necessarily reduced, which has the effect of reducing the percentage of error of a measurement.

Therefore, the measurement error due to the projection remains small because the depth (approximately 100 nm) is very small compared with the surface size (4608 nm × 3456 nm). This makes the contribution to the total dislocation length along the z axis small compared with the lengths along the x and y axes.

The third measurement artifact arises from the fact that if dislocations overlap, the total dislocation length will be underestimated. Indeed, the total dislocation length is calculated using $L = N_t \times P_s$, where N_t is the number of dislocation pixels identified and P_s is the pixel size.

If two dislocations overlap, the area of overlapping will be counted only once, whereas it should be counted twice. Therefore, for a higher density, the potential overlapping is higher, and thus, the measurement error is higher. As an estimate, the so-called apparent dislocation density was calculated using $\rho_{apparent} = \frac{N_t * P_s}{V \times E}$, where E is the thickness of a dislocation in number of pixels, N_t is the total number of dislocation pixels, and P_s is the size of a pixel in nanometers.

To visualize the effect of overlapping, the real density contained in the volume is plotted as a function of the apparent density in Fig. 12.

As expected, the difference between the real density and the apparent density increases with increasing dislocation density. The apparent density deviates by a few percent for densities below 4×10^{13} m^{-2} and by 20% for densities close to 10^{14} m^{-2}, which is close to the maximum achievable densities.

As a conclusion, the main source of measurement error comes from the overlapping of dislocations, with a higher density resulting in a
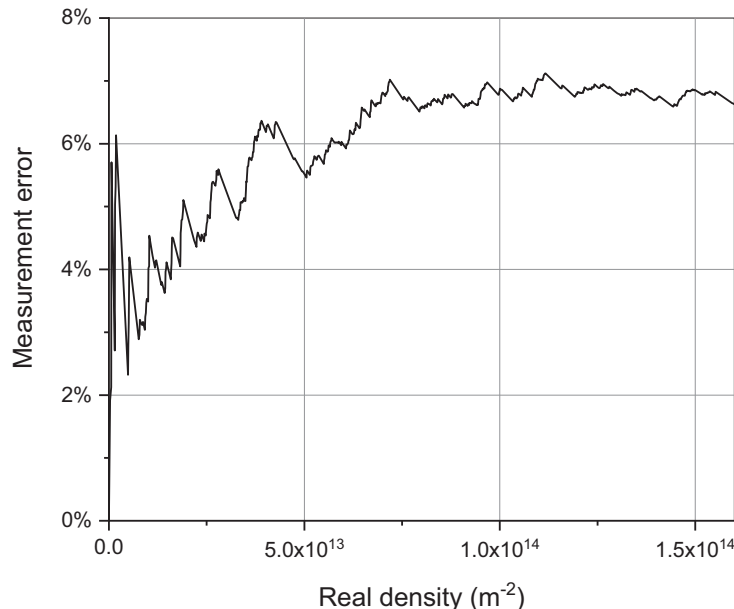

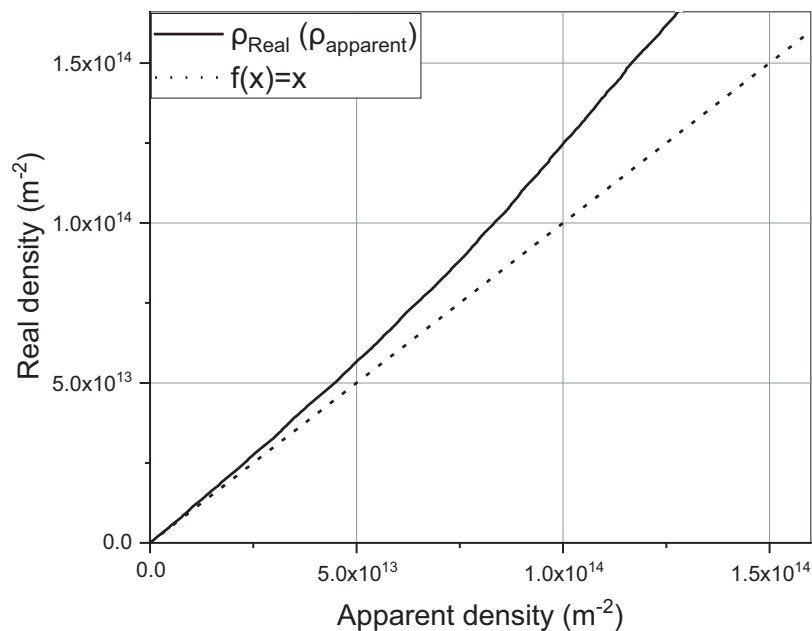**Fig. 11.** Measurement error between the real and projected density.

Fig. 12. Representation of the real dislocation density, obtained in a three-dimensional volume, as a function of the apparent density obtained on a projected image of the volume. The divergence that appears comes from the phenomenon of overlapping dislocations.

higher measurement error. For highly deformed materials, the maximum density achievable using the method is close to 10^{14} m^{-2}, for which an error of 20% due to potential overlapping is present.

In Fig. 13, the results obtained during this study on the two grains characterized with the clustering method (Fig. 9) are presented. The measurement obtained with clustering (in green, Fig. 13) calculated from the series of BSE images is compared with a traditional N/S measurement (in blue, Fig. 13) measured on a single BSE image per dislocation observation condition. Considering the different sources of measurement error presented previously, the results obtained are comparable in their order of magnitude and the measurement uncertainties are superimposed.

4. Discussion

The method presented in this study indicates that it is possible to measure dislocation densities semi-automatically on deformed materials

by switching to a local average of the grain intensity profile around the analyzed pixel.

This methodology was tested on several duplex samples, and the analysis on a deformed grain was performed on an austenite grain in which the dislocations were relatively easy to image with little noise, thus facilitating the post-processing steps by clustering. Having fewer sharp dislocations with more noise can lead to an additional loss of information during the comparison of intensity profiles because the local average will be distorted. Nevertheless, this problem can be avoided because the first step of the method allows a "feature map" to be obtained, which highlights in green all the profiles of the pixels showing a substantial difference with the neighboring profiles. It is therefore sufficient to determine the minimum size of the clusters to be analyzed to remove all the pixels that do not form a dislocation. The method, however, remains dependent on the quality of the acquired images and the polishing state of the material, which must be perfect.

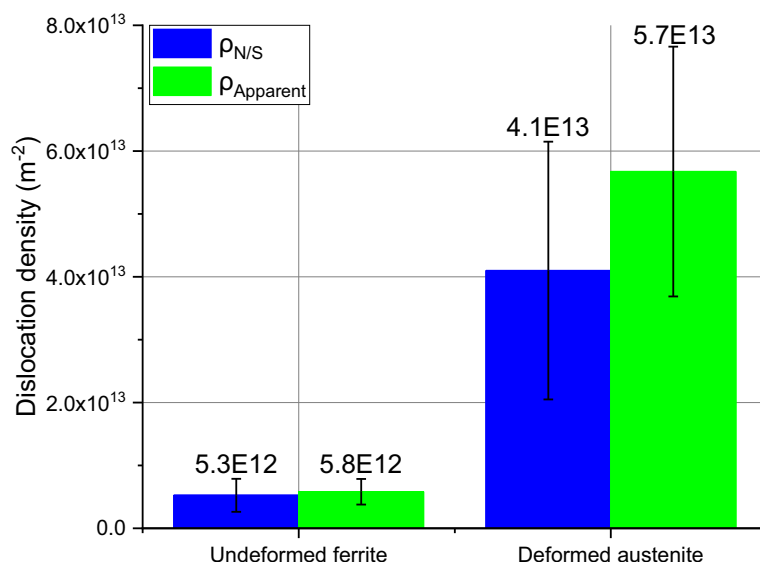It was demonstrated by calculation that dislocation densities in the

Fig. 13. Representation of the dislocation density measured for two different grains: a non-deformed ferrite grain and a 3% deformed austenite grain. The measure of dislocation density obtained by clustering (in green) is compared with another measure (in blue) taken directly from the images, which consists of dividing the total number N of dislocations visible on the image by the surface of this image. (For interpretation of the references to colour in this figure legend, the reader is referred to the web version of this article.)

range of 10^{12} m^{-2} to 1.2×10^{14} m^{-2} can be precisely measured. These limits correspond to dislocation density measurements in the literature for undeformed steels. For example, Ruggles et al. [14] observed densities between 10^{13} and 10^{14} m^{-2} in an austenitic sample, as did Zaefferer et al. [8], who reported a dislocation density of 2×10^{13} m^{-2}. Higher densities are expected in deformed steels, as measured by ECCI and TEM by Gutierrez-Urrutia et al. [28], who observed densities ranging between $10 \pm 4 \times 10^{13}$ and $17 \pm 6 \times 10^{13}$ m^{-2}. In addition, Bissey-Breton et al. [29] observed a dislocation density of 4.2×10^{13} m^{-2} in a recrystallized bulk. In semiconductors, the measured density has been reported to range between 10^{11} and 10^{13} m^{-2} [30,31]. Even if the minimum densities are lower than those calculated and measured in this study, it should be noted that the highest densities for semiconductors were measured using XRD, for which the issue of dislocation overlap that can occur in imaging is not observed, as XRD does not allow observation of the dislocations.

It is nevertheless important to specify that these boundary measurements consider values inherent to the observed materials; such as the apparent thickness E and the explored volume, which are both dependent on the material and the crystallographic orientation. During this study, several different materials were examined. Images recorded in the same conditions allowed to measure apparent thickness E for copper (22 ± 2) nm, ferrite (30 ± 2) nm, austenite (32 ± 2) nm, and nickel (27 ± 2) nm. Moreover, in ECCI images, the apparent thickness E of the dislocations may also depend on the observation conditions of the sample, as reported by Kriaa et al. [32], who obtained an apparent thickness of 30 and 19 nm on the same dislocation, depending on the channeling conditions selected.

This study has shown that the measurement error due to the orientation of the dislocations relative to the surface is negligible and that the main source of uncertainty originates from the overlap of dislocations as the dislocation density increases. It gives a measurement error of approximately 3% for low densities of approximately 10^{13} m^{-2} and 20% for the limit densities of 10^{14} m^{-2} achievable with this method. This uncertainty, due to the overlap of dislocations, also exists for dislocation densities measured from TEM images. Considering a typical TEM image, with a surface size of 4008×2664 pixels, a pixel size of 0.55 nm, and a dislocation width of 6.5 nm, the uncertainty is approximately 5% for densities close to 10^{14} m^{-2} and can increase to 20% for maximum densities of 3×10^{14} m^{-2}. The precision of the measurement is thus drastically better for TEM *vs.* SEM-ECCI, as for the same density, the SEM results in an uncertainty of 20%, whereas that for TEM is only 5%. This is mainly because the higher spatial resolution of TEM allows the dislocations to be better discriminated. However, TEM is more localized than SEM, and the question of representativeness can always arise.

The second major source of error originates from the apparent thickness of the dislocations E, obtained from BSE images, which were measured at one-pixel accuracy, resulting in a measurement error of 6% to 7%. When added to the other contribution to the measurement error, the total measurement error for 10^{12} m^{-2} is 15% and it is 34% for 10^{14} m^{-2}.

Two examples were provided, the first on an undeformed ferrite grain, where the measured dislocation density was $5.8 \pm 0.6 \times 10^{12}$ m^{-2}, and the second on a 3% deformed austenite grain, where the measured dislocation density was $5.7 \pm 1.1 \times 10^{13}$ m^{-2}.

Finally, the main source of error is associated with the explored depth, which is directly related to the probed volume. The calculations were here performed considering the deepest condition in each miniseries (around 150 nm). However, the theoretical value of $3\xi_g$ varies within an image miniseries. As an example, it varies from 70 nm (g_{111}) to 150 nm (g_{311}) for austenite. But, surprisingly, we observed that the number of visible dislocations was quite similar for the different conditions, *i.e.* for the different theoretical analyzed depth. For those reasons, the uncertainty of the quantitative measure is yet about the order of magnitude. However, when comparing different deformed states, for the same material acquired under the same experimental conditions, the

measurement uncertainty shall be close to the one previously calculated (15 to 34%). A better quantification of the explored depth is thus necessary, and could be determined experimentally by the stereo pairs method [11,33], or by combining TEM and SEM observations of the same sample. Picard et al. [34] simulated ECCI images as a function of the explored thickness. A comparison between simulated and experimental images could help to specify the explored volume for this orientation. Moreover, the data treatment procedure could be improved by taking into account the nature of the Kikuchi bands crossed, which is theoretically possible as each intensity profile is a signature of the orientation [19].

This measurement error affects the mechanical properties, which depend on the dislocation density. Blaizot et al. [2] provided an expression of the yield strength, proportional to $\sqrt{\rho_0}$, where ρ_0 is the initial density, which implies that a measurement error of 10% on the dislocation density, for an undeformed material, changes the yield strength by $\pm 5\%$. For a material with a dislocation density close to 10^{14} m^{-2}, where the measurement error on the density is 20%, the calculated yield strength will have an error of $\pm 10\%$.

Future studies will be conducted to determine the place of this method in relation to other techniques used to obtain dislocation density measurements such as TEM, DRX, or EBSD. Eventually, the combination of this detection method and the eCHORD technology could be applied for the simultaneous characterization of several undeformed or deformed alloy grains, simultaneously characterizing their orientation, dislocation density, and nature.

5. Conclusion

In this study, an approach to measure dislocation density in deformed materials was presented along with the measurement uncertainty induced by the method. Using a data-classification algorithm based on a local average of the grain around the analyzed pixel, it became possible to obtain a quantitative measure of the dislocation density in a deformed sample without knowing the grain orientation. Moreover, from the imaging data, it was possible to calculate the measurement uncertainties of this method.

The ranges of densities that can be reached are on the order of 10^{10} m^{-2} for semiconductors and can increase to 10^{14} m^{-2} for steels. The main sources of error are the explored volume and the superposition of dislocations. It was also possible to determine the evolution of the error caused by the superposition of dislocations as well as that originating from the apparent thickness of dislocations present in the images. The uncertainty of measurement for these last two points is 27% at most on the highest densities characterizable using this method. This uncertainty does not consider the error made on the analyzed volume. Indeed, a change in the value of ξ_g can lead to errors on the analyzed volume of 20 to 70%. However, when comparing different deformed states of the same material acquired in the same experimental conditions, the experimental uncertainty in the density evolution shall be the one that we estimated during this study.

In summary, the R-ECCI method coupled with clustering enabled characterization of the dislocation densities in a material, specifically in a deformed material with the presence of local disorientation. The method is relevant for the study of heterogeneous microstructures that require imaging but also for multiphase materials.

Objective of the paper

Present dislocation density measurable using ECCImages and the automatic detection tool presented in Cazottes et al. 2019 and the corresponding measurement uncertainty

Declaration of Competing Interest

The authors declare that they have no known competing financial interests or personal relationships that could have appeared to influence the work reported in this paper.

Data availability

Data will be made available on request.

Acknowledgements

References

[1] E. Nadgornyi, Dislocation dynamics and mechanical properties of crystals, Prog. Mater. Sci. 31 (1988) 1–530.

[2] J. Blaizot, THESE de DOCTORAT DE L'UNIVERSITE DE LYON - Etude de l'influence des procédés de fabrication sur les propriétés mécaniques des alliages de Nickel, 2015.

[3] J. Blaizot, T. Chaise, D. Nélias, M. Perez, S. Cazottes, P. Chaudet, Constitutive model for nickel alloy 690 (Inconel 690) at various strain rates and temperatures, Int. J. Plast. 80 (2016) 139–153.

[4] P. Diano, A. Muggeo, J.C. Van Duysen, M. Guttmann, Relationship between microstructure and mechanical properties of Alloy 690 tubes for steam generators, J. Nucl. Mater. 168 (3) (1989) 290–294.

[5] Y. Meng, X. Ju, X. Yang, The measurement of the dislocation density using TEM, Mater. Charact. 175 (2021) 111065.

[6] G. Dini, R. Ueji, A. Najafizadeh, S.M. Monir-Vaghefi, Flow stress analysis of TWIP steel via the XRD measurement of dislocation density, Mater. Sci. Eng. A 527 (10–11) (2010) 2759–2763.

[7] Z. Zribi, H.H. Ktari, F. Herbst, V. Optasanu, N. Njah, EBSD, XRD and SRS characterization of a casting Al-7wt% Si alloy processed by equal channel angular extrusion: dislocation density evaluation, Mater. Charact. 153 (2019) 190–198.

[8] S. Zaefferer, N.-N. Elhami, Theory and application of electron channelling contrast imaging under controlled diffraction conditions, Acta Mater. 75 (Aug 2014) 20–50, https://doi.org/10.1016/j.actamat.2014.04.018.

[9] D.R. Clarke, A. Howie, Calculations of lattice defect images for scanning electron microscopy, Philos. Mag. 24 (190) (Oct 1971) 959–971, https://doi.org/10.1080/14786437108217060.

[10] P. Morin, M. Pitaval, D. Besnard, G. Fontaine, Electron–channelling imaging in scanning electron microscopy, Philos. Mag. A 40 (4) (Oct 1979) 511–524, https://doi.org/10.1080/01418617908234856.

[11] B.A. Simkin, M.A. Crimp, Dislocation Detection Depth Measurements in Silicon Using electron Channelling Contrast Imaging, San Francisco Press, Inc, San Francisco, CA (United States), 1996.

[12] A.J. Wilkinson, G.R. Anstis, J.T. Czernuszka, N.J. Long, P.B. Hirsch, Electron channelling contrast imaging of interfacial defects in strained silicon-germanium layers on silicon, Philos. Mag. A 68 (1) (1993) 59–80.

[14] T.J. Ruggles, Y.S.J. Yoo, B.E. Dunlap, M.A. Crimp, J. Kacher, Correlating results from high resolution EBSD with TEM-and ECCI-based dislocation microscopy: approaching single dislocation sensitivity via noise reduction, Ultramicroscopy 210 (2020), 112927.

[15] M.A. Crimp, Scanning electron microscopy imaging of dislocations in bulk materials, using electron channeling contrast, Microsc. Res. Tech. 69 (5) (2006) 374–381.

[16] B.E. Dunlap, T.J. Ruggles, D.T. Fullwood, B. Jackson, M.A. Crimp, Comparison of dislocation characterization by electron channeling contrast imaging and cross-correlation electron backscattered diffraction, Ultramicroscopy 184 (2018) 125–133.

[17] H. Mansour, J. Guyon, M.A. Crimp, N. Gey, B. Beausir, N. Maloufi, Accurate electron channeling contrast analysis of dislocations in fine grained bulk materials, Scr. Mater. 84–85 (Aug 2014) 11–14, https://doi.org/10.1016/j.scriptamat.2014.03.001.

[18] G. L'hôte, et al., Rotational-Electron channeling contrast imaging analysis of dislocation structure in fatigued copper single crystal, Scr. Mater. 162 (Mar. 2019) 103–107, https://doi.org/10.1016/j.scriptamat.2018.10.050.

[19] C. Lafond, T. Douillard, S. Cazottes, P. Steyer, C. Langlois, Electron CHanneling ORientation Determination (eCHORD): an original approach to crystalline orientation mapping, Ultramicroscopy 186 (Mar. 2018) 146–149, https://doi.org/10.1016/j.ultramic.2017.12.019.

[20] S. Cazottes, et al., Toward an automated tool for dislocation density characterization in a scanning electron microscope, Mater. Charact. 158 (Dec. 2019) 109954, https://doi.org/10.1016/j.matchar.2019.109954.

[21] M.-S. Chen, J. Han, P.S. Yu, Data mining: an overview from a database perspective, IEEE Trans. Knowl. Data Eng. 8 (6) (1996) 866–883.

[22] A.K. Jain, Data clustering: 50 years beyond K-means, Pattern Recogn. Lett. 31 (8) (2010) 651–666.

[23] A.K. Jain, M.N. Murty, P.J. Flynn, Data clustering: a review, ACM Comp. Surveys (CSUR) 31 (3) (1999) 264–323.

[24] F.A. De Carvalho, Y. Lechevallier, Partitional clustering algorithms for symbolic interval data based on single adaptive distances, Pattern Recogn. 42 (7) (2009) 1223–1236.

[25] E. Diday, Y. Lechevallier, M. Schader, P. Bertrand, B. Burtschy, New Approaches in Classification and Data Analysis, Springer Science & Business Media, 2013.

[28] I. Gutierrez-Urrutia, D. Raabe, Dislocation density measurement by electron channeling contrast imaging in a scanning electron microscope, Scr. Mater. 66 (6) (Mar. 2012) 343–346, https://doi.org/10.1016/j.scriptamat.2011.11.027.

[29] S. Bissey-Breton, J. Gravier, V. Vignal, Impact of superfinish turning on surface integrity of pure copper, Proc. Eng. 19 (2011) 28–33.

[30] J.K. Hite, P. Gaddipati, D.J. Meyer, M.A. Mastro, C.R. Eddy, Correlation of threading screw dislocation density to GaN 2-DEG mobility, Electron. Lett. 50 (23) (2014) 1722–1724.

[31] C. Shang, et al., A pathway to thin GaAs virtual substrate on on-axis Si (001) with Ultralow Threading Dislocation density, Phys. Status Solidi A 218 (3) (2021) 2000402.

[32] H. Kriaa, A. Guitton, N. Maloufi, Fundamental and experimental aspects of diffraction for characterizing dislocations by electron channeling contrast imaging in scanning electron microscope, Sci. Rep. 7 (1) (2017) 1–8.

[33] L.A. Jácome, K. Pöthkow, O. Paetsch, H.-C. Hege, Three-dimensional reconstruction and quantification of dislocation substructures from transmission electron microscopy stereo pairs, Ultramicroscopy 195 (2018) 157–170.

[34] Y.N. Picard, M. Liu, J. Lammatao, R. Kamaladasa, M. De Graef, Theory of dynamical electron channeling contrast images of near-surface crystal defects, Ultramicroscopy 146 (Nov. 2014) 71–78, https://doi.org/10.1016/j.ultramic.2014.07.006.